ARTICLE

Check for updates

Astronomical forcing shaped the timing of early Pleistocene glacial cycles

Yasuto Watanabe[1,2,8], Ayako Abe-Ouchi [1,2,3,4✉], Fuyuki Saito [4], Kanon Kino [1,9], Ryouta O'ishi [1], Takashi Ito [5,6], Kenji Kawamura [3,4,7] & Wing-Le Chan [1,10]

Glacial cycles during the early Pleistocene are characterised by a dominant 41,000-year periodicity and amplitudes smaller than those of glacial cycles with ~100,000-year periodicity during the late Pleistocene. However, it remains unclear how the 41,000-year glacial cycles during the early Pleistocene respond to Earth's astronomical forcings. Here we employ a three-dimensional ice-sheet model to simulate the glacial cycles at ~1.6–1.2 million years before present and analyse the phase angle of precession and obliquity at deglaciations. We show that each deglaciation occurs at every other precession minimum, and when obliquity is large. The lead-lag relationship between precession and obliquity controls the length of interglacial periods, the shape of the glacial cycle, and the glacial ice-sheet geometry. The large amplitudes of obliquity and eccentricity during this period helped to establish robust 41,000-year glacial cycles. This behaviour is explained by the threshold mechanism determined by ice-sheet size and astronomical forcings.

[1] Atmosphere and Ocean Research Institute, The University of Tokyo, Kashiwa, Japan. [2] Department of Earth and Planetary Science, Graduate School of Science, The University of Tokyo, Tokyo, Japan. [3] National Institute of Polar Research, Tokyo, Japan. [4] Japan Agency for Marine-Earth Science and Technology, Yokohama, Japan. [5] Center for Computational Astrophysics, National Astronomical Observatory of Japan, Tokyo, Japan. [6] Planetary Exploration Research Center, Chiba Institute of Technology, Narashino, Japan. [7] Department of Polar Science, The Graduate University for Advanced Studies, SOKENDAI, Tokyo, Japan. [8] Present address: Meteorological Research Institute, Japan Meteorological Agency, Tsukuba, Japan. [9] Present address: Department of Civil Engineering, Graduate School of Engineering, The University of Tokyo, Tokyo, Japan. [10] Present address: Japan Agency for Marine-Earth Science and Technology, Yokohama, Japan. ✉email: abeouchi@aori.u-tokyo.ac.jp

Analyses of deep-sea sediment cores and other paleoclimatic archives have documented the glacial-interglacial climate cycles during the Pleistocene, which is linked to the ice-sheet dynamics driven by the variation in astronomical forcings[1–8]. One of the outstanding problems on the glacial-interglacial cycles is that the main periodicity of glacial–interglacial cycles shifted from 41 kyr in the early Pleistocene (>1.2 Ma) to 100 kyr in the late Pleistocene (<0.8 Ma) (the transition known as the Middle Pleistocene Transition, MPT) (Fig. 1d)[9,10]. Across the MPT, the amplitude of the glacial cycles increased from ~70 m to ~120 m (sea level equivalent; SLE)[5–7]. The time series of the glacial cycles exhibits an asymmetry characterised by a slow glaciation and rapid deglaciation (sawtoothed shape), more pronounced in the late Pleistocene than in the early Pleistocene (Fig. 1d)[2,11]. It has been shown that, during the late Pleistocene, the variation in climatic precession (~20-kyr periodicity; Fig. 1a) played a key role in driving the sawtoothed glacial cycles and determining the timing of deglaciations in conjunction with obliquity forcing (41-kyr periodicity; Fig. 1b) in establishing the 100-kyr glacial cycles[10,12–16].

During the early Pleistocene, on the other hand, only a weak variance is observed in the periodicity of climatic precession (Fig. 1a) and the periodicity of obliquity dominates the glacial cycle, which constitutes the so-called 41-kyr problem[17–22]. Several mechanisms have been proposed to resolve the 41-kyr problem, including the anticorrelation between the strength of

summer insolation and the length of summer[19,20] and the offset of the 20-kyr component between the variations of the Northern Hemisphere (NH) and Southern Hemisphere (SH) ice sheets[21,22]. While the signals from precession are relatively difficult to detect compared to obliquity owing to its short periodicity, the precessional variability in early Pleistocene cycles has been identified in recent studies using paleoclimate proxies with orbitally-independent age models[23–25]. In addition, the existence of asymmetry in the cycles (i.e., fast deglaciation) has been inferred for pre-MPT periods[4,26–28]. Although the role of precession in determining deglaciations of pre-MPT periods is unclear, it has been recently shown that, using records of North Atlantic ice rafting, deglaciations occur at minima in the climatic precession, even during pre-MPT periods[29]. However, the relative contributions of obliquity and precession in determining the timings of terminations of the 41-kyr glacial cycles and the duration of interglacials have not been quantitatively elucidated.

Here, we employ the IcIES-MIROC model, a dynamic three-dimensional NH ice-sheet model, IcIES, coupled with a climate parameterization based on results from a general circulation model, MIROC (Supplementary Fig. 1)[12]. In this model, the climate change over the NH land, driven by changes in astronomical forcings, is estimated by using a climate parameterization based on a suite of experiments using discrete GCM snapshots[30]. The surface temperature is given to the ice-sheet model as a climate forcing[12]. This setup allows us to represent both fast feedbacks (water vapour, cloud, sea-ice, and vegetation feedbacks) and slow feedbacks (albedo/temperature/ice-sheet, and lapse-rate/temperature/ice-sheet feedbacks). Previously, the model successfully reproduced the 100-kyr glacial cycles for the last 400 kyr[12]. In this study, the climate parameterization used in IcIES–MIROC is improved by taking into account vegetation feedback at NH high latitudes (Supplementary Figs. 1 and 2 and Supplementary Table 1)[31–33]. Using this model, we simulate the glacial cycles during ~1.6–1.2 Ma (from Marine Isotope Stage, MIS, 53 to 36; Table 1), when 41-kyr glacial cycles are clearly observed in the $\delta^{18}O$ signature (blue-hatched area in Fig. 1d). This period corresponds to the largest amplitudes in eccentricity (Fig. 1a), obliquity (Fig. 1c), and the 41-kyr component of the $\delta^{18}O$ signature[27] under atmospheric CO_2 levels comparable to those of the late Pleistocene (Fig. 1c). This makes this period ideal for investigating the role of astronomical forcings in driving the 41-kyr glacial cycles. We discuss the roles of obliquity and precession in determining the timing of deglaciation, the shape of the time series of glacial cycles, ice-sheet geometry, and the periodicity of the 41-kyr glacial cycles.
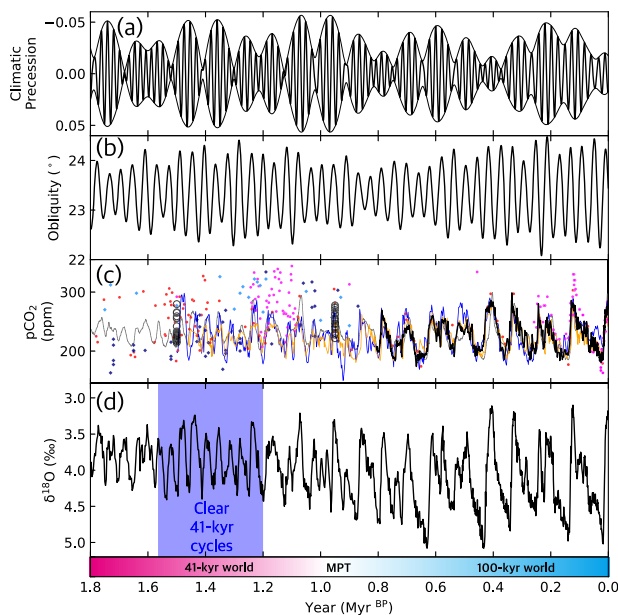

Fig. 1 Time series of Earth's astronomical forcings and glacial cycles for the last 1.8 Myr. a Time series of climatic precession ($e \sin \omega$, where e is eccentricity and ω is the angle from the moving vernal equinox of the Earth to its perihelion)[77,82], where the envelope corresponds to eccentricity[77]. **b** Time series of obliquity[77]. **c** Reconstructions of atmospheric pCO_2 based on Antarctic ice cores (black line)[83], Alan Hill blue ice (black circles)[34], alkenones (light-blue diamonds), $\delta^{13}B$ signature of planktonic foraminifera (pink dots: *Globigerinoides ruber*; red dots: *Trilobatus sacculifer*), paleosols (dark-blue diamonds) (the above data are summarised by Köhler and van de Wal[84]; see references therein), leaf-wax $\delta^{13}C$ signature recorded in the sediment cores at the Bay of Bengal (orange line)[38], and $\delta^{13}C$ signature of deep-sea sediment cores (blue line)[37], and $\delta^{18}O$-based inverse estimate using a theoretical model (grey line)[36]. **d** Records of the globally-stacked benthic $\delta^{18}O$ signature of 57 sediment cores[3]. The blue hatched area represents the period of focus in this study (1.565–1.2 Ma), which exhibits 41-kyr cycles clearly.

Results

Simulating the glacial cycles from MIS 53 to 36. We first conduct a numerical experiment using a combination of realistic variations in astronomical forcings and a constant CO_2 forcing ($pCO_2 = 230$ ppm, representative of the estimated pCO_2; Fig. 1c)[34–39] to identify the role of combined astronomical forcings in driving the glacial cycles during the early Pleistocene. The time series of the forcings and the simulated ice volume are shown and compared with the oxygen isotope ($\delta^{18}O$) signals from the deep sea in Fig. 2. The most striking feature of the result is that, even with constant pCO_2, the 41-kyr glacial cycles of the NH ice volume are clearly simulated between MIS 53 and 36. This result indicates that the response of the ice-sheet dynamics to the variations in astronomical forcings in the NH high latitudes primarily drives the 41-kyr glacial cycles.

The timing of each deglaciation and the shape of each glacial cycle in our simulation are very similar to the $\delta^{18}O$ signature during this period (Fig. 2f), despite the $\delta^{18}O$ signature reflecting not

Table 1 List of IcIES–MIROC experiments conducted in this study.

| Time period (kyr[BP])	Obliquity	Eccentricity	Atmospheric pCO$_2$	Major appearances in figures	Remarks
1565–1200	Realistic	Realistic	Constant (230 ppm)	Figs. 2–6	Standard run
1565–1200			Variable (van de Wal et al.[36])	Fig. 2	–
1500–1200			Variable (Lisiecki[37])	Fig. 2	–
400–0	Realistic	Realistic	Constant (190 ppm)	Spp. Fig. 9	–
			Constant (230 ppm)	Spp. Figs. 7, 9	–
			Variable (Bereiter et al.[83])	Fig. 5c, Spp. Fig. 11	–
			Variable (Bereiter et al.[83])	Spp. Fig. 11	w/o vegetation feedback
1600–1200	Realistic	Realistic	Constant (190 ppm)	Spp. Fig. 9	–
			Constant (210 ppm)	Spp. Fig. 9	–
			Constant (230 ppm)	Spp. Fig. 9	–
			Constant (250 ppm)	Spp. Fig. 9	–
			Constant (270 ppm)	Spp. Fig. 9	–
1565–1200	60% amplitude	Realistic	Constant (230 ppm)	Fig. 7	–
1565–1200	Realistic	0.6 × (realistic)	Constant (230 ppm)	Fig. 7	–
		0.2 × (realistic)			–
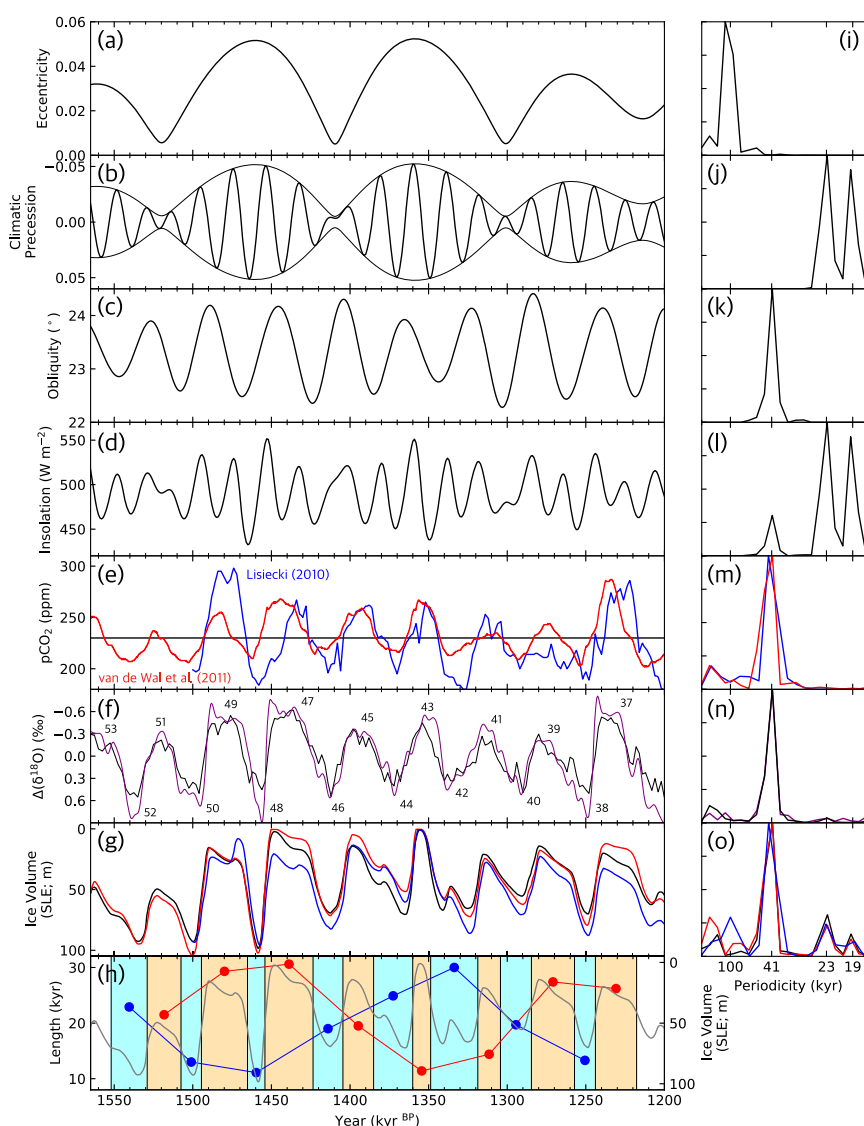
Fig. 2 Time series of forcing and responses of Northern Hemisphere ice sheets. a–g Time series across the period of interest and **i–o** corresponding normalised amplitude spectra, respectively. **a** Eccentricity[77]. **b** Climatic precession, where the envelope corresponds to eccentricity[77]. **c** Obliquity[77]. **d** Insolation at 65°N on June 21[77]. **e** CO$_2$ forcing used as model input: constant value of 230 ppm (black) and variable CO$_2$ (red: van de Wal et al.[36], blue: Lisiecki[37]). **f** δ^{18}O signature relative to the mean value of this period (black: Lisiecki and Raymo (2005)[3], purple: U1308 core[8]). Data from Hodell et al.[8] were filtered using a zero-phase low-pass Butterworth filter. **g** Simulated North American and Eurasian ice sheet volume (unit: m, in sea level equivalent; SLE) calculated with different CO$_2$ forcings, shown in the same colours as in (**e**). **h** Duration of each glacial/interglacial period (blue/red lines) under a constant CO$_2$ concentration of 230 ppm.
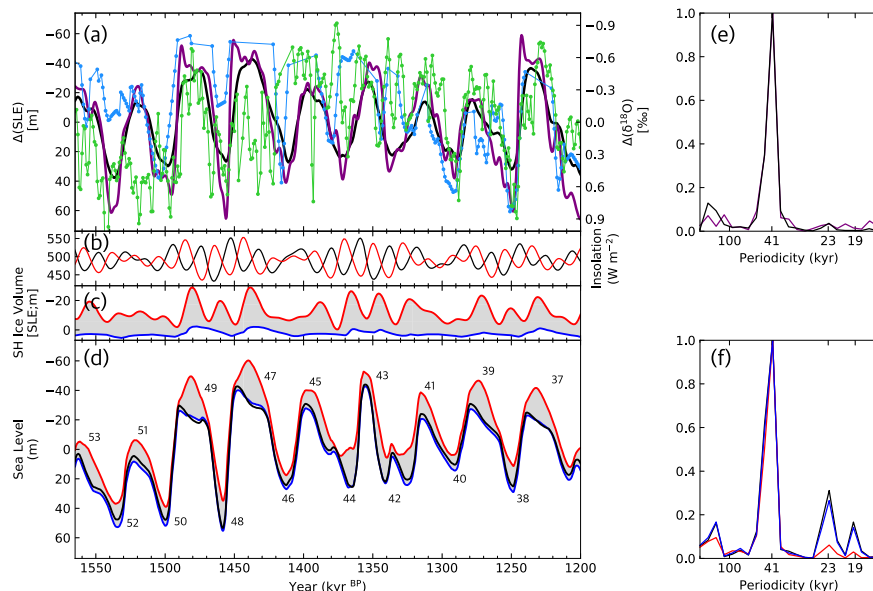
Fig. 3 Time series of reconstructed past sea level and the calculated sea level change. a–d Time series across the period of interest. **a** Sea-level proxy (green: Elderfield et al.[6], blue: Rohling et al.[7]) and $\delta^{18}O$ signature relative to the mean value of this period (black: Lisiecki and Raymo[3], purple: U1308 core[8]). Data from U1308 core[8] are filtered using a zero-phase low-pass Butterworth filter. Data from Lisiecki and Raymo[3] are converted to sea level based on the method described in Spratt and Lisiecki[85]. **b** Insolation at 65°N on June 21 and 65°S on Dec 21 (black and red lines, respectively). **c** The simulated Southern Hemisphere (SH) ice sheet volume from de Boer et al.[40] and Raymo et al.[21] (blue and red lines, respectively) (unit: m, in sea level equivalent; SLE). **d** Calculated past sea level (unit: m) for both SH ice-sheet variations in (**c**) using the same colours, and for no SH ice sheet (black line), with Northern Hemisphere (NH) ice-sheet variation under a constant CO_2 concentration of 230 ppm. The sea level reference (zero value) is set to the mean value of the NH ice sheet SLE. **e, f** The normalised amplitude spectra for (**a**) and (**d**), respectively.

only the ice volume but also deep ocean temperature[3,8]. For example, the lengths of interglacial periods from the longest (e.g., MIS 49, 47 and 37) to the shortest (MIS 41) are consistent with those in the $\delta^{18}O$ record (Fig. 2f, Supplementary Fig. 3c, d) (see 'Methods' for the definition). We summarise the characteristics of the ice volume time series and the lengths of the glacial and interglacial periods (blue and red lines, respectively) in Fig. 2h. The boundaries between the interglacial and glacial periods are defined as the mid-point of the maximum and minimum ice volume for each deglaciation that is observed in the $\delta^{18}O$ signature (see 'Methods' and Supplementary Table 2). Results indicate that the lengths of the interglacial and glacial periods are inversely correlated. In other words, when an interglacial period is long, the following glacial period tends to be short, and vice versa. The power spectrum of the simulated ice volume shows a strong 41-kyr signal with weaker 23- and 19-kyr signals (black line in Fig. 2g), which is consistent with the high-resolution data from the North Atlantic (U1308 core site; purple line in Fig. 2f; Supplementary Fig. 3d)[8]. The simulated deglaciations occur within a relatively short interval, i.e., less than 15 kyr (Supplementary Fig. 3e), which is also consistent with the observed trend for the rapid deglaciation during the early Pleistocene[26–28].

To compare our results with reconstructions of sea level, we add estimates of the variations in the volume of the SH ice sheet, namely the Antarctic ice sheet, by Raymo et al.[21] and de Boer et al.[40] (red and orange lines, respectively, in Fig. 3c) to those of our NH ice sheet (black line in Fig. 3d). The work by Raymo et al.[21] proposed an offset between the NH and SH ice volumes, with a large variation in SH ice volume of up to ~30 m at MIS 48 (Fig. 3c red line). On the other hand, recent simulations of the SH ice sheet using a sophisticated ice-sheet model suggest that the amplitude of the variations in SH ice sheet was at most ~15 m sea level equivalent during the deglaciations from MIS 50 and 48[40–42]. Despite the non-negligible amplitude of SH ice-sheet variation, the amplitude of global sea-level variation is almost as large as that of

the NH ice sheet alone (Fig. 3c, red and blue lines). The amplitude of the simulated sea-level change ranges between ~50–95 m, which is consistent with the range shown in the reconstructions (~60–90 m; green and blue lines in Fig. 2a)[6,7]. These results reinforce the idea that the 41-kyr glacial cycles are caused primarily by the variations in the NH ice sheet owing to the variations in astronomical forcings. By considering the variations in the SH ice sheet simulated in these studies, the power spectrum of the variation in the modelled global sea level shows a clear dominance at 41-kyr periodicity even with a precession signal weaker than that of the NH ice volume alone, because of the anti-phased precession signal in the SH (Fig. 3b, d)[21,22].

To elucidate the role of orbital-scale variability in pCO_2 (i.e. the carbon cycle) in establishing the 41-kyr glacial cycles, we conduct further experiments using the published pCO_2 variations (red and blue lines in Fig. 2e)[36,37]. We use two reconstructions based on an inverse modelling approach applied to $\delta^{18}O$ records[36] and a method based on the $\delta^{13}C$ gradient between the deep Pacific and intermediate North Atlantic[37]. The results with these non-constant pCO_2 reconstructions exhibit little difference from the simulation with constant pCO_2 (230 ppm) in terms of the shape and the amplitude of the glacial cycles (Fig. 2g). The timing of the deglaciation and the dominance of the 41-kyr periodicity are also almost identical. Thus, it could be inferred that the establishment of the 41-kyr periodicity, shape, and amplitude of the glacial cycles at ~1.6–1.2 Ma are determined primarily by the variations in astronomical forcing (Fig. 2a–d, g). Below, we further analyse the model results with constant pCO_2 (230 ppm) to understand the fundamental role of astronomical forcings in shaping the 41-kyr glacial cycles.

Shapes of the 41-kyr glacial cycles and the astronomical forcings. To quantify the contribution of each astronomical forcing (obliquity and precession) that determines the timing of
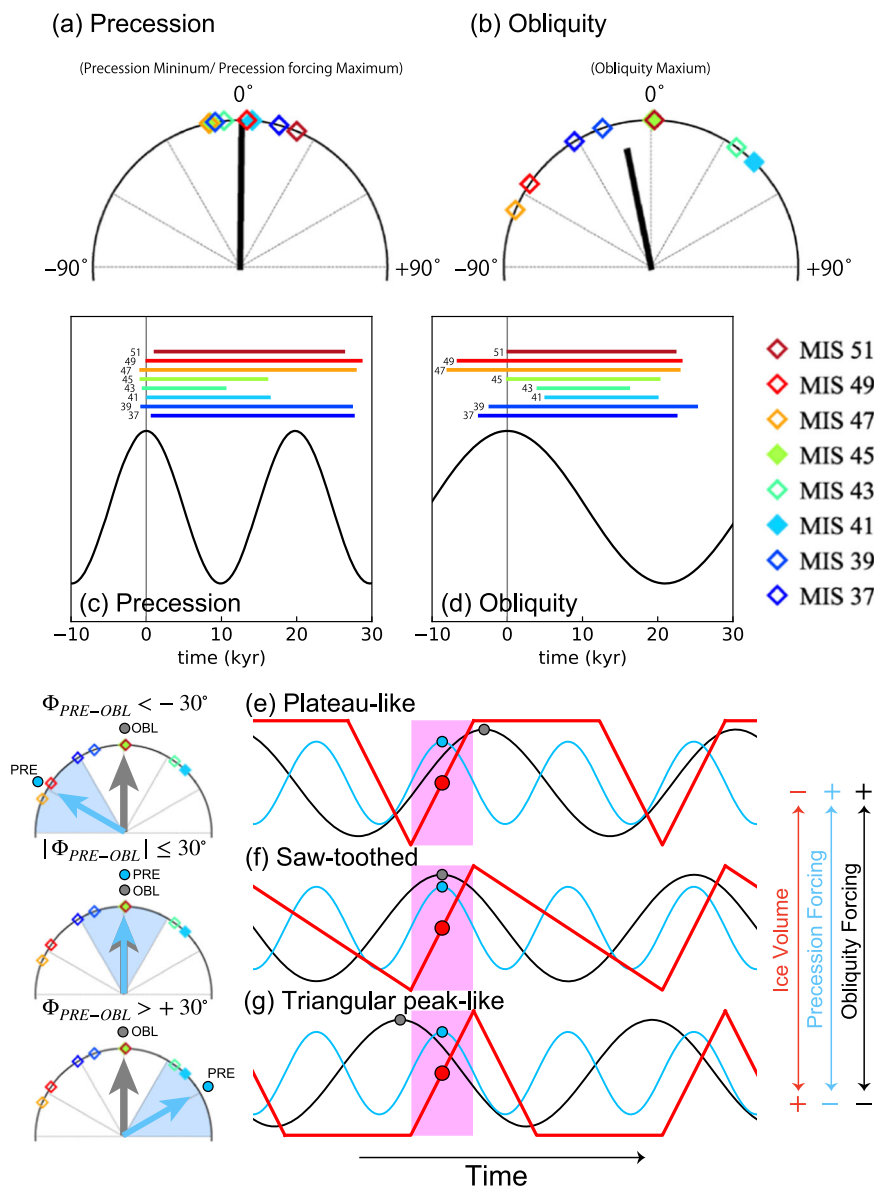
Fig. 4 Shapes of glacial cycles in relation to phase angle of precession and obliquity forcings at deglaciations. a, b Phase wheels showing the phase angles at corresponding deglaciations in the standard experiment run with a constant atmospheric pCO_2 of 230 ppm. The right/left domains correspond to positive/negative values. Lengths and angles of the black lines represent the Rayleigh's R values and mean phase angles, respectively. Rayleigh's R values for our deglaciations are 0.98 for precession and 0.80 for obliquity, indicating precession-controlled deglaciations. **c, d** Timing of onset and termination of interglacials in relation to an idealised variation in astronomical forcings, following Tzedakis et al.[45] (see 'Methods'). **e–g** Relative phase angle between precession and obliquity forcings ($\Phi_{PRE-OBL}$) is <30° (**e**), ~0° (**f**), and >+30° (**g**), as represented by the angle between cyan and grey arrows in each phase wheel of obliquity. Schematic of the characteristics of the time series of the 41-kyr glacial cycle (red line: ice sheet volume) are shown with corresponding astronomical forcings (precession and obliquity) for two 41-kyr glacial cycles. Black and cyan lines denote obliquity and precession, respectively. The classification of the shapes of the glacial cycles and their relationship with each phase angle ($\Phi_{PRE-OBL}$) in (**e–g**) is also summarised in Supplementary Table 2.

deglaciation in our simulation, we conduct a phase analysis of obliquity and precession forcings at the deglaciations (see 'Methods')[27]. In Fig. 4a, b, the so-called phase wheels for obliquity and precession, respectively, are shown. These phase wheels summarise the phase angle of the astronomical forcing at each deglaciation (see also Supplementary Fig. 4), in a unit circle (diamonds in Fig. 4a, b)[27,43]. The average phase angle of both precession and obliquity, represented by the direction of the thick black line, is around zero, showing that the deglaciation occurs mostly at precession minima (maxima of precession forcing) and obliquity maxima. This result infers that both obliquity and precession forcings pace the deglaciations of the 41-kyr glacial

cycles, consistent with the discussions on the 100-kyr glacial cycles during the late Pleistocene[10,12,13,44]. While the phase angles of precession are tightly concentrated around 0° for all deglaciations investigated in this study, i.e., from −12° to +23° (Fig. 4a), those of obliquity are spread over a wider range, i.e., from −67° to +44° (Fig. 4b), suggesting that precession is crucial in determining the precise timing of deglaciation.

The phase relation between obliquity and deglaciation appears to control the length of the following interglacials. In order to analyse the relationship between the length of interglacial periods and the phase angles of precession and obliquity, the beginning and end of all simulated interglacials relative to the variations in

5

precession and obliquity are shown in the coloured lines in Fig. 4c, d, respectively. The onset of the interglacials occurs at the maxima of precession forcing (Fig. 4a, c). The duration of the interglacial periods ranges from 10 to 30 kyr (i.e., 0.5–1.5 precession cycles). For MIS 45, 43 and 41, the interglacial periods end within one precession cycle ($\lesssim$20 kyr), while, for MIS 51, 49, 47, 39 and 37, they continue beyond one precession cycle ($\gtrsim$20 kyr). As shown in Fig. 4d, the duration of an interglacial that starts earlier than an obliquity maximum is long (i.e., MIS 49, 47, 39 and 37), whereas it is short when the interglacial starts after an obliquity maximum (i.e., MIS 43 and 41). The end of interglacial periods occurs around the minima of the obliquity and precession forcings, while the timing of the onset of the interglacials is determined strongly by the maxima of precession forcing (Fig. 4c). Thus, when the maximum of precession forcing occurs before (after) the obliquity maximum, the interglacials tend to be longer (shorter) than one precession cycle. In other words, the length of an interglacial period is controlled by the lead–lag relationship between the maxima of obliquity and precession forcings.

The phase angle of obliquity at a maximum of precession forcing, $\Phi_{\text{PRE–OBL}}$, is denoted by the direction of cyan arrows in Fig. 4e–g. On the right-hand side of Fig. 4e–g, three typical glacial cycles (plateau-like, sawtoothed, and triangular peak-like) are shown schematically as red lines, together with idealised obliquity (black line) and precession (cyan line) forcings. When $\Phi_{\text{PRE–OBL}}$ is around zero ($-30° \leq \Phi_{\text{PRE–OBL}} \leq 30°$), a sawtoothed glacial cycle is formed (MIS 51–50, 45–44, and 37–36 in Fig. 4f; Supplementary Table 2). When $\Phi_{\text{PRE–OBL}}$ is negative ($<-30°$), a plateau-like glacial cycle is formed (MIS 49–48, 47–46, and 39–38 in Fig. 4e), while when it is positive ($>+30°$), a triangular peak-like glacial cycle is formed (MIS 43–42 and 41–40 in Fig. 4g). This classification is also summarised in Supplementary Table 2. The relationship is strikingly similar to that found in the analysis of the relative phases of obliquity and precession at deglaciations and the length of interglacials of the 100-kyr world[45]. This implies that the impact of the relative phase angle of obliquity and precession controls the length of interglacials, and hence the shapes of glacial cycles through a common mechanism associated with the ice-sheet dynamics triggered by variations in the astronomical forcings. The physical basis of the relationship between the shapes of glacial cycles and phase of obliquity and precession is evaluated later in this study.

Ice-sheet geometry and the astronomical forcings. The ice sheet distribution for each glacial maximum in the experiment with constant $p\text{CO}_2$ (230 ppm) is shown in Fig. 5a, b, and Supplementary Fig. 5. In most glacial maxima, the Laurentide and

Cordilleran ice sheets are separated and the southern margin does not extend beyond the Great Lakes. In one case (MIS 48 in Fig. 5b), the Laurentide and Cordilleran ice sheets are merged and the resulting glacial ice sheet covers a large area of the continent, including the Great Lakes. The glacial cycle with the maximum areal distribution (MIS 48) corresponds to a case categorised as a long interglacial and plateau-like glacial cycle. The ice sheet at the glacial maximum of MIS 48 is geographically extensive and thin, because it expands quickly within half a precession cycle and retreats before the North American (NA) ice sheet reaches equilibrium (see Supplementary Movie 1). This ice sheet is much thinner than the Last Glacial Maximum (LGM) ice sheet (Fig. 5a, c, and Supplementary Fig. 6). At this glacial maximum, the change in the insolation is large owing to the high eccentricity and the decreases in precession and obliquity forcings, which allows the rapid expansion of the NA ice sheet. Here, the relative phase angle of obliquity and precession corresponds to the plateau-like glacial cycle in Fig. 4e. At this glacial maximum, the southern edge of the NA ice sheet reaches the Mississippi drainage basin[18,46]. This ice-sheet distribution is similar to the reconstruction of the maximum ice sheet which reached Missouri, USA, at ~2.5 Ma[47] and 1.31 ± 0.13 Ma[48]. The MIS 48 in our model (1.458 Ma) is slightly out of the range of uncertainty in the latter record, and so the maximum distribution at MIS 48 in our model may not explain this reconstruction. Nonetheless, our results indicate that the ideal condition for achieving an extensive NH ice sheet is a combination of high eccentricity and a relative phase angle of obliquity and precession corresponding to a plateau-like glacial cycle. If a thick regolith layer had covered the NA continent before the MPT, the NA ice sheet might have extended over an even larger area of the continent[9,47–50]. In such a case, one of the plateau-like glacial cycles such as the one which encompasses MIS 38 would have resulted in an extensive NA ice sheet as in reconstructions[48].

Deglaciation of the 41-kyr glacial cycles and the astronomical forcings. To understand why the glacial cycles of the NH ice sheet terminate every 41 kyr, we compare the three consecutive cycles from MIS 47 to 41 with the steady-state response of an ice sheet to astronomical forcing (Fig. 6a, d; see also Supplementary Fig. 7). The steady-state response of an ice sheet to the surface temperature anomaly due to insolation and CO_2 was derived in our previous study[12]. The cyan and magenta lines represent the steady-states achieved if the model is initiated from a small and large NA ice volume, respectively, showing a hysteresis behaviour within the approximate range of -4 to 2 K (grey hatched area). The ice sheet gains mass if the temperature anomaly falls below the lower branch of the hysteresis curve (cyan line) and it loses
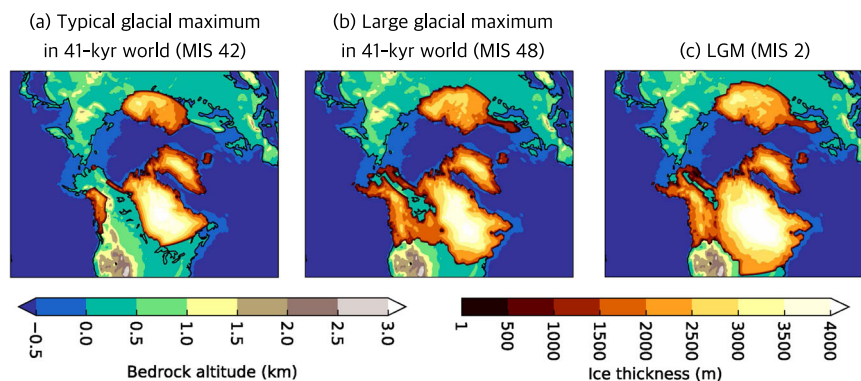

(a) Typical glacial maximum in 41-kyr world (MIS 42)   (b) Large glacial maximum in 41-kyr world (MIS 48)   (c) LGM (MIS 2)

Bedrock altitude (km)
−0.5 0.0 0.5 1.0 1.5 2.0 2.5 3.0

Ice thickness (m)
1 500 1000 1500 2000 2500 3000 3500 4000

Fig. 5 Simulated North American ice sheet distribution. Simulated North American ice sheet distribution for each glacial maximum for **a** a typical glacial maximum (MIS 42) and **b** a large glacial maximum (MIS 48) under a constant $p\text{CO}_2$ (230 ppm), and **c** Last Glacial Maximum (LGM, 21 ka) with realistic variations in atmospheric CO_2[83].
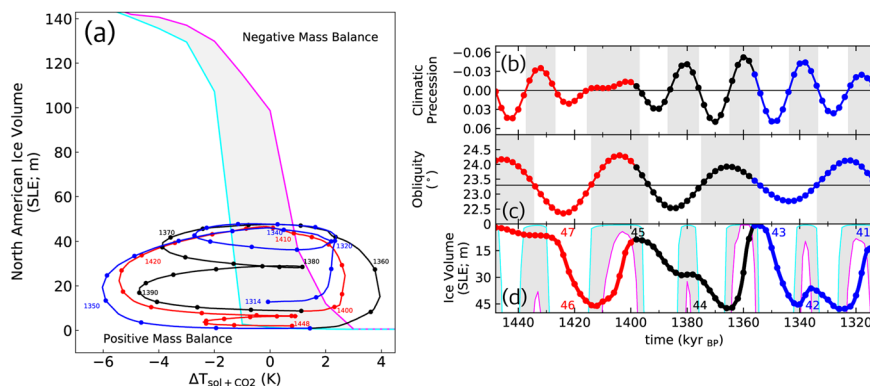
Fig. 6 Hysteresis of steady states and transient evolution of the North American ice sheet. Magenta/cyan lines denote large/small volume steady states when the model run starts with large/small initial ice sheets[12]. **a** Plot showing equilibrium mass and surface mass balances of the North American ice sheets according to temperature anomalies relative to the present value. Lines with dots at 2-kyr intervals represent the transient evolution of the ice volume from Marine Isotope Stage (MIS) 47 to 45 (red), from 45 to 43 (black), and from 43 to 41 (blue) using the standard experiment run with a constant atmospheric pCO$_2$ of 230 ppm. **b–d** Time evolution of climatic precession, obliquity and North American ice sheet volume, respectively. Grey shading represents periods when precession is below average or when obliquity is above average.

mass if the temperature anomaly rises above the upper branch (magenta line). These lower and upper branches correspond to the thresholds of ice-sheet growth and retreat, respectively. In order to understand the initiation of the 41-kyr glacial cycles, we compare the results of the transient variation, shown as trajectories, before the MPT for the period from MIS 47 to 41 to the steady-state response.

For the typical 41-kyr cycles with a sawtooth shape (MIS 45–43; black lines in Fig. 6a, d), ice-sheet retreat occurs once in every two precession cycles. At the first insolation maximum (~1380 ka) after the onset of the glacial cycle, the intensity of insolation is insufficient to exceed the threshold of termination (upper branch of the hysteresis curve, magenta line in Fig. 6a). This is because the effects of precession and obliquity forcings cancel each other (Fig. 6b, c), so that the ice sheet continues to grow. The second local maximum of insolation (~1360 ka) is strong because it is compounded by the contributions from both obliquity and precession. Owing to this compound effect from the obliquity and precession forcings, the summer insolation provides sufficient time for a rapid retreat of the NA ice sheet. After crossing the upper threshold, the ice sheet starts to lose mass at ~1364 ka because the ice sheet is larger than that at the first local insolation maximum, in addition to the strong insolation. The combined effect of ice-sheet size and insolation allows the temperature to exceed the threshold, and thus triggers the onset of deglaciation (black lines in Fig. 6a, d). Once deglaciation has commenced, feedback from the glacial isostatic rebound assists in complete deglaciation until an interglacial state is reached (Supplementary Fig. 8)[12]. As a result, the deglaciation occurs once in two precession cycles through a threshold mechanism that results from the hysteresis response of the ice sheet, as in the late Pleistocene. This is consistent with an analysis of the timing of early Pleistocene complete deglaciations and astronomical forcing, which suggests that the 41-kyr cycle arises because every second insolation peak is boosted by above-average obliquity[51]. Our results demonstrate that the nonlinear response of the ice-sheet dynamics to the astronomical forcing supports the occurrence of deglaciations at every 41-kyr.

For the glacial cycle from MIS 47 to 45, the interglacial period is longer than one precession cycle (red lines in Fig. 6a, d). The ice sheet does not develop at the first minimum of precession forcing (maximum of precession), but it does develop rapidly at the second. In contrast, the interglacial period is short in the case of the cycle from MIS 43 to 41 (blue lines in Fig. 6a, d). The ice sheet starts to

develop soon after the previous deglaciation at the first minimum of precession forcing (maximum of precession), and the glacial period continues for more than one precession cycle. In all three cases, the deglaciation occurs once in two precession cycles through the threshold mechanism. The differences between the shapes of the 41-kyr glacial cycles (red and blue lines in Fig. 6d) reflect the phase relation between obliquity and precession.

Sensitivity studies on the role of astronomical and CO$_2$ forcings. In order to understand the effect of the amplitudes of obliquity and eccentricity (i.e., the amplitude of precession forcing) on the 41-kyr glacial cycles at ~1.6–1.2 Ma, we conduct additional sensitivity tests using a set of artificially modified astronomical forcings. We reduce the amplitudes of eccentricity to 60 and 20% (Fig. 7a), representing the large variations in the amplitudes of the 100-kyr eccentricity cycles (Fig. 1a). We also reduce the amplitudes of obliquity to 60% (Fig. 7d), which is similar to the amplitudes during its smallest period (e.g., 1.0–0.6 Ma; Fig. 1b). When the amplitude of eccentricity is reduced, the 100-kyr periodicity of the ice volume intensifies (blue and red lines in Fig. 7a). For the case of 20% eccentricity amplitude (red line in Fig. 7a), only deglaciations from MIS 50, 46 and 40 are reproduced. Owing to the small eccentricity, other deglaciations are not reproduced and the ice sheet continues to develop. This result is consistent with the previous observation that the strength of the 100-kyr periodicities in δ^{18}O proxies and eccentricity are intermittently correlated throughout the Pliocene and Pleistocene[52]. The low 100-kyr power during ~1.6–1.2 Ma would have been a result of the deglaciations at each 41-kyr owing to the ice-sheet responses driven by obliquity and precession forcings. With a decreased obliquity amplitude (60% as shown by the red line in Fig. 7d), the glacial cycles also show 100-kyr periodicity (red line in Fig. 7f).

To clarify the relative importance of the astronomical forcings to the mean levels of pCO$_2$ for the period ~1.6–1.2 Ma, we conduct a set of calculations with different constant values of atmospheric pCO$_2$ (190, 210, 230, 250 and 270 ppm) (Supplementary Fig. 9a). In all cases, the 41-kyr periodicity dominates the glacial cycles and the 100-kyr signal is not enhanced even under the lowest constant atmospheric pCO$_2$ (190 ppm). In contrast, the lowest constant pCO$_2$ (190 ppm) enhances the 100-kyr variability at 0.4–0 Ma (Supplementary Fig. 9b). It seems that the impact of lowering the constant atmospheric pCO$_2$ on the periodicity of the
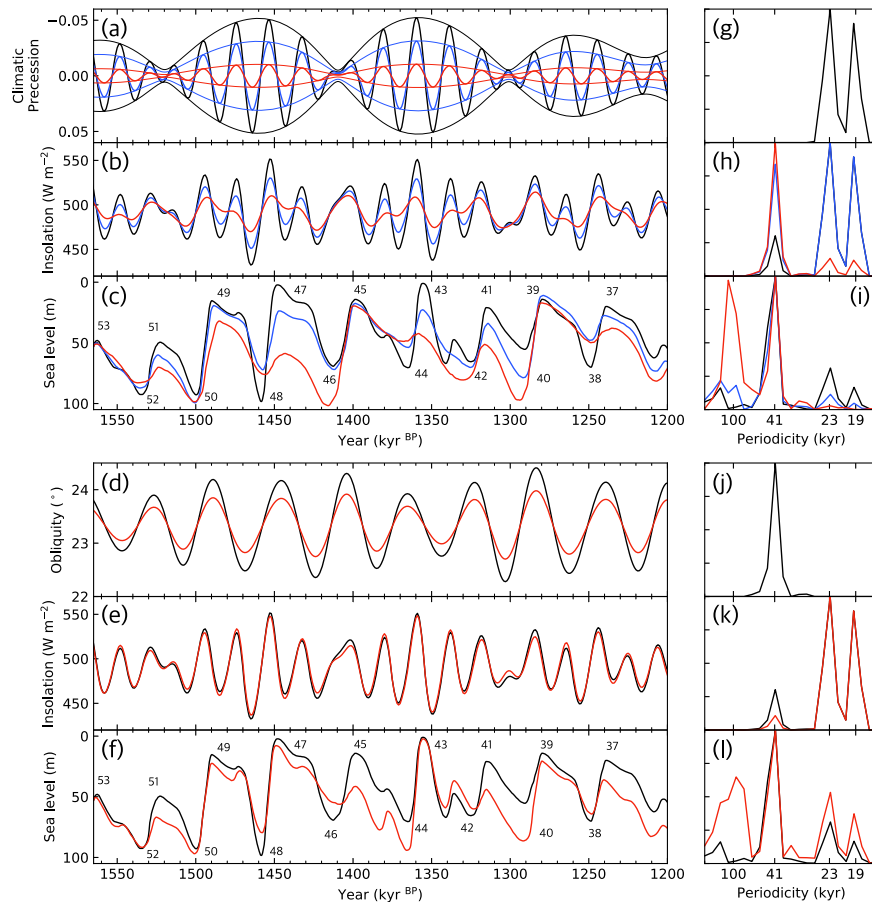
Fig. 7 Time series of forcings and response of Northern Hemisphere ice sheets to modified astronomical forcings. a–f Time series across the period of interest and **g–l** corresponding normalized amplitude spectra, respectively. **a** Climatic precession, where the envelope corresponds to eccentricity[77] is scaled by 1.0 (black), 0.6 (blue) and 0.2 (red). **b** Insolation at 65°N on June 21[77]. **c** Simulated Northern Hemisphere ice-sheet volume (unit: m, in sea level equivalent, SLE) for astronomical forcings in a, using the same colours. **d** Obliquity[77] scaled by 1.0 (black) and 0.6 (red). **e** Insolation at 65°N on June 21[77]. **f** Simulated Northern Hemisphere ice-sheet volume (unit: m, in SLE) for the astronomical forcings in (**d**) using the same colours. These calculations are conducted with a constant atmospheric pCO$_2$ of 230 ppm as in the standard experiment run.

glacial cycle is different between the period of ~1.6–1.2 Ma and the last 0.4 Myr, depending on the astronomical forcing, i.e., the amplitude of eccentricity. A further enhancement of the 100-kyr periodicity with a realistic atmospheric pCO$_2$, shown by the grey line in Supplementary Fig. 9b, indicates the importance of the interaction between the ice sheets, climate, and atmospheric pCO$_2$ for the last 0.4 Myr.

Discussion

In this study, we investigate the roles of obliquity and precession in establishing 41-kyr glacial cycles and show their importance in driving deglaciations, and producing different glacial ice-sheet extent and different shapes of the glacial cycles using a state-of-the-art three-dimensional ice-sheet model. We show that the precession forcing plays an important role in driving the glacial cycles before the MPT: (1) the precession forcing determines the timing of the threshold for deglaciation, while obliquity also supports the deglaciations of the 41-kyr glacial cycles; (2) the lead–lag relationship between precession and obliquity forcings determines the length of the interglacials and the shape of the glacial cycles; and (3) a thin and extensive NA ice sheet forms and retreats within one precession cycle when eccentricity is sufficiently large. These findings quantitatively support the recent discussions suggesting the importance of precession forcing on climate variability during the early Pleistocene[18,23–25,29]. The variations in the SH ice sheet may help to completely weaken

signals from the ~20 kyr periodicity of precession forcing from sea-level records during the early Pleistocene[21,22]. Our results indicate that the orbital-scale variability of CO$_2$ forcing has a relatively minor role at ~1.6–1.2 Ma in driving the 41-kyr glacial cycles compared with the astronomical forcings. This is in contrast to the role of the CO$_2$ forcing in the late Pleistocene, when the orbital-scale variability of CO$_2$ forcing amplifies the variations in the ice volume as shown in our previous study[12].

We show that the relative phase relationship between obliquity and precession forcings determines the lengths of interglacial and glacial periods, and hence the shape of the time series of the 41-kyr glacial cycle (i.e., plateau-like cycle at MIS 49–48, 47–46, and 37–36, sawtoothed cycle at MIS 51–50, 45–44, and 39–38, and triangular peak-like cycle at MIS 43–42 and 41–40). This is consistent with past literature that discusses the 100-kyr world during the late Pleistocene and the lengths of interglacial periods[45,53–56]. For example, the categorisation of the shapes of 41-kyr glacial cycles is similar to the previous discussion on the lengths of interglacials in the 100-kyr world[45]: a long interglacial in the plateau-like glacial cycle is similar to MIS 11c, and a short interglacial in the triangular peak-like glacial cycle is similar to MIS 7e. This implies that a common mechanism driven by astronomical forcing controls deglaciation, interglacial duration, and onset of glaciation in both the early Pleistocene and late Pleistocene.

We show that the 41-kyr glacial cycles are driven by the threshold mechanism that drives the 100-kyr glacial cycles during

the late Pleistocene. In the early Pleistocene, the NA ice sheet reaches the threshold for deglaciation within ~41 kyr when the mass balance becomes negative, such that ice sheet retreats rapidly and the glacial period terminates at each 41-kyr cycle, whereas it takes ~100 kyr for the NA ice sheets to reach the threshold during the late Pleistocene. The difference in periodicity is partly attributable to the strength of the astronomical forcings: large eccentricity (i.e., strong precession forcing) and strong obliquity forcing at ~1.6–1.2 Ma.

We also quantitatively show that the amplitude modulations of both eccentricity and obliquity contribute to a change in the dominant periodicity of the NH ice-sheet mass using a 3-D ice-sheet model. These results support the hypothesis that the amplitude modulation of the astronomical forcings can contribute to the periodicity modulation of the glacial cycles[52,57], and hence to the occurrence of the MPT. Our experiment period (~1.6–1.2 Ma) corresponds to the period of the largest amplitude in eccentricity during the Quaternary[52], which is associated with the amplitude modulation of eccentricity with a periodicity of ~2.4 Myr[58–60]. This period also corresponds to a large amplitude in obliquity due to the 1.2-Myr amplitude modulation of obliquity[58–60]. We find that if the amplitudes of obliquity and eccentricity are not as large as what they were during ~1.6–1.2 Ma, then the glacial cycle exhibits a 100-kyr periodicity instead of a 41-kyr periodicity if other conditions are kept the same. However, the changes in the amplitude of astronomical forcings still cannot fully explain the evolution of the dominant periodicity of glacial cycles throughout the Pleistocene, including the MPT. Small eccentricity and small amplitudes in obliquity appear even before ~1.6 Ma in the 41-kyr world. This may imply that a process or feedback previously unconsidered helps to achieve a dominant 41-kyr periodicity before the MPT, such as the long-term change in CO$_2$[38,39,61–68] and the removal of the old surface regolith layer on the NA continent[9,47,49]. Nonetheless, our simulations at ~1.6–1.2 Ma clearly demonstrate that the amplitude of astronomical forcings is an important factor affecting the periodicity of glacial cycles. On top of such unconsidered feedbacks as the long-term change in CO$_2$ and the removal of regolith, a decline in the amplitude of both eccentricity and obliquity can contribute to triggering the transition of the dominant periodicity of glacial cycles.

To fully understand the Earth system dynamics throughout the Quaternary including the MPT, further investigation using a global climate-ice sheet-carbon cycle modelling approach would be necessary[50,65,66], with consideration of the long-term modulation of astronomical forcings[52,57], variations in pCO$_2$[10,12,44,50,67,68], and the removal of continental regolith[9,47–50]. In addition, the ocean circulation may have been important in driving the variations in the oceanic carbon cycle (i.e. atmospheric pCO$_2$) during the glacial periods, and hence in initiating deglaciation[65,69,70]. This means that the coupling of the ocean circulation and the climate is also a process that potentially affects the evolution of the system during the glacial-interglacial periods. Thus, high-resolution CO$_2$ and climate reconstructions beyond the MPT, e.g. from Antarctic ice cores[16,34,71,72] and deep-sea sediment cores[38,39,61–64,73], together with global climate-ice sheet-carbon cycle modelling are highly desirable.

Methods

Ice-sheet model coupled with climate parameterization (IcIES-MIROC). We employ the three-dimensional dynamic ice-sheet model coupled with a climate parameterization based on results from a general circulation model, IcIES-MIROC[12,30]. The ice-sheet model couples ice-sheet dynamics to the surface mass balance and bedrock deformation. The primitive inputs to the model are the variations in insolation (i.e., astronomical forcings) and atmospheric pCO$_2$, which are transformed into changes in the surface temperature field in the ice-sheet model. The ice-sheet model used in this study is essentially the same as that used in Abe-Ouchi et al. (2013) except for some improvements, including the climate

parameterization. Vegetation–temperature feedback is known to play an important role when warming/cooling occurs through boreal forest/tundra replacement. This is not only the case for annual mean global warming caused by greenhouse gas increase, but also for the insolation and temperature increase in summer season due to changes in obliquity and precession. This was demonstrated using the MIROC climate model in the Holocene 6 ka experiment and the Last Interglacial (LIG) 127 ka experiment[74,75]. It is further shown that the obliquity is up to 1.5 times more effective than climatic precession in regulating the summer temperature change per the same insolation change by our numerical calculations using our climate model, MIROC-LPJ (see Supplementary Methods). We take this feedback into account when considering the relationship between insolation and surface temperature in running the ice-sheet model, IcIES-MIROC.

Climate parameterization with vegetation feedback. The climatic effects of the changes in astronomical forcings, i.e., insolation (ΔT_{sol}), pCO$_2$ (ΔT_{CO2}), and ice sheet size attributable to the lapse rate and surface albedo feedback (ΔT_{ice}) are included separately. $\Delta T_{nonlinear}$ represents a residual term due to other feedback effects and is set to zero[12]:

$$T_s = T_{ref} + \Delta T_{sol} + \Delta T_{CO2} + \Delta T_{ice} + \Delta T_{nonlinear} \qquad (1)$$

These terms are parameterized based on GCM snapshots[30] using the MIROC AGCM[76]. The ice-sheet model used in this study is essentially the same as that in Abe-Ouchi et al.[12] except for an improvement in the modification of the temperature change with vegetation-temperature feedback due to the variation in insolation. This is based on the analysis of a large set of experiments using MIROC-LPJ (see Supplementary Methods), by taking into account vegetation–temperature feedback through boreal forest/tundra exchange[33,75] and by comparing with previous AGCM snapshots (Supplementary Fig. 10)[12]:

$$\Delta T_{sol} = \Delta T_{N65} + \Delta T_{veg}, \qquad (2)$$

where ΔT_{N65} corresponds to the temperature anomaly due to summer insolation, Q (i.e., June 21 at 65°N):

$$\Delta T_{N65} = \frac{Q - 490}{40} \times 3.25 + 1.0757 \qquad (3)$$

The second term in Eq. 2 (ΔT_{veg}) represents the larger amplification of the surface temperature due to changes in obliquity, rather than precession, through boreal forest/tundra exchange (see Supplementary Fig. 2 and the Supplementary Methods)[33,75]:

$$1.5 \times (OBL - 23.446), \ (Q \le 520)$$

$$\Delta T_{veg} = 1.5 \times \frac{530 - Q}{530 - 520} \times (OBL - 23.446), \ (520 < Q < 530)$$

$$0, \ (Q \ge 530), \qquad (4)$$

where OBL is obliquity (°). This formulation reflects the fact that under comparatively warm climate conditions, the vegetation feedback at high latitudes disappears (Supplementary Fig. 2)[31,33,75]. The NA surface temperature and the simulated ice volumes with the inclusion of the new parameterization are compared with the previous configuration[12] for the last 400 kyr in Supplementary Fig. 11. The reproduction of the local minimum in ice volume at MIS 3 and the deglaciation from MIS 2 is improved after ΔT_{veg} is included (Supplementary Fig. 11g). For more information on the parameterization of vegetation feedback, see Supplementary Methods. All other model configurations, including parameterizations for the surface accumulation and the ablation, are the same as in our previous model in Abe-Ouchi et al.[12].

Experimental design. The astronomical forcings of Berger and Loutre[77] are used to calculate the variations in insolation. The experiments are extended from MIS 53 (1565 ka) to MIS 36 (1200 ka), corresponding to the period during which the 40-kyr cycles are evident in the proxy records (Fig. 2f)[3,8]. The experiments are conducted using constant pCO$_2$ concentration (230 ppm) as a control run. Although there is no direct high-resolution pCO$_2$ reconstruction available from ice cores for the target period (Fig. 1c), there are indirect pCO$_2$ reconstructions based on inversion techniques using a climate model[36] (red line in Fig. 2e) and from a modified δ^{13}C gradient between the deep Pacific and intermediate North Atlantic[37] (blue line in Fig. 2e). These indirect reconstructions are reasonably consistent with the existing fragmented direct reconstructions before the MPT[39,78]. This study includes experiments using these reconstructions to ascertain the effect of variations in pCO$_2$. The power spectrum of the inputs and the simulated ice volumes is calculated using the *SciPy*[79] periodogram function and the Hamming window.

The initial conditions at 1565 ka are set as an interglacial with a comparatively large ice sheet, as determined by previous experiments. This is based on the relatively small value in the δ^{18}O signature (Fig. 2f) of MIS 53 and 51 in comparison to MIS 49 or 47. However, the results of the experiments with different initial conditions reveal that the dependence on the initial conditions disappears no later than MIS 50 (Supplementary Fig. 12). Therefore, although analysis before MIS 50 should be treated with caution, it is considered that this dependence does not affect the results, either qualitatively or quantitatively. Because the pCO$_2$

reconstruction from Lisiecki[37] is limited before 1500 ka, the output of the control run at 1500 ka is used as the initial conditions.

The time series of the NH ice sheet in the control run is compared with the steady-state response of the NH ice sheet using a set of different climate forcing ($\Delta T_{sol} + \Delta T_{CO_2}$) obtained in the previous study[12]. We note here that the steady state of the NH ice sheet exhibits a hysteresis response for a certain range of the climate forcing ($\Delta T_{sol} + \Delta T_{CO_2}$), which was obtained in the work of Abe-Ouchi et al. (2013)[12]. The transient response of the NA ice sheet in this study is shown at every 2 kyr in Fig. 6a.

Phase analysis of astronomical forcings. We calculate Rayleigh's R (Eq. 5)[27,43,80] to quantify the phase stability with respect to different astronomical forcings[51]:

$$R = \frac{1}{N} \left| \sum_{n=1}^{N} \cos \phi_n + \sin \phi_n \right|, \qquad (5)$$

where N is the total number of deglaciation events (eight in this study) and ϕ_n is the phase angle of the astronomical forcings sampled at the n-th deglaciation[27]. Rayleigh's R takes a maximum value of 1.0 when the sampled phases are all the same[27]. The phase angle of each astronomical forcing was calculated via wavelet analysis using the MATLAB toolbox[81], and the wavelet phase angles at 19.8121 and 41.9803 kyr were adopted for precession and obliquity, respectively, both of which satisfactorily represent the variations in each astronomical forcing in this experimental period. The phase angles of precession and obliquity forcings are shown in Supplementary Fig. 4a, b (black lines). Phase zero corresponds to the maximum contribution to the insolation (local maxima for precession/obliquity forcing). The phase angle at each deglaciation shows the lead–lag relationship between each deglaciation and the astronomical forcings. The timings of glaciation/deglaciation are defined as the time when the ice volume reaches the mean value of the maximum and minimum ice volumes before and after glaciation/deglaciation, corresponding to the observed variations in the $\delta^{18}O$ signature (vertical lines in Fig. 2h and diamonds in Supplementary Fig. 4c). The duration of the glacial (cyan shading in Fig. 2h) and interglacial periods (orange shading in Fig. 2h) are clearly defined by the boundaries. For MIS 42, we define the glacial maximum as the local maximum at 1325 ka, not at 1341 ka, following the maximum of the NA ice sheet. We note that this analysis is a comparison between obliquity and precession, including an analysis of proxy records, and is not of a statistical nature. The definition of the onset and termination of the interglacials is identical to that shown in Fig. 2h. The lengths of the interglacials in Fig. 4c, d are slightly different from those shown in Fig. 2h because of the fit to the idealised astronomical forcings.

Data availability
The source data for graphs and charts are available from the following website: https://cesd.aori.u-tokyo.ac.jp/cesddb/publication/index.html.

Code availability
The code for IcIES associated with this study is available from the corresponding author (A.A.). MIROC–LPJ is not publicly archived following the copyright policy of the MIROC community. For further information, please contact the corresponding author (A.A.).

References
1. Milankovitch, M. *Kanon der Erdbestrahlung und Seine Anwendung auf das Eiszeit-Problem* (R. Serbian Acad., 1941).
2. Hays, J. D., Imbrie, J. & Shackleton, N. J. Variations in the earth's orbit: Pacemaker of the ice ages. *Science* **194**, 1121–1132 (1976).
3. Lisiecki, L. E. & Raymo, M. E. A Pliocene-Pleistocene stack of 57 globally distributed benthic δ18O records. *Paleoceanography* **20**, PA1003 (2005).
4. Bintanja, R. & van de Wal, R. S. W. North American ice-sheet dynamics and the onset of 100,000-year glacial cycles. *Nature* **454**, 869–872 (2008).
5. Sosdian, S. & Rosenthal, Y. Deep-sea temperature and ice volume changes across the Pliocene-Pleistocene climate transitions. *Science* **325**, 306–310 (2009).
6. Elderfield, H. et al. Evolution of ocean temperature and ice volume through the mid-Pleistocene climate transition. *Science* **337**, 704–709 (2012).
7. Rohling, E. J. et al. Sea-level and deep-sea-temperature variability over the past 5.3 million years. *Nature* **508**, 477–482 (2014).
8. Hodell, D. A. & Channell, J. E. T. Mode transitions in Northern Hemisphere glaciation: co-evolution of millennial and orbital variability in Quaternary climate. *Clim. Past* **12**, 1805–1828 (2016).
9. Clark, P. U. et al. The middle Pleistocene transition: characteristics, mechanisms, and implications for long-term changes in atmospheric pCO₂. *Quat. Sci. Rev.* **25**, 3150–3184 (2006).
10. Raymo, M. E. The timing of major climate terminations. *Paleoceanography* **12**, 577–585 (1997).
11. Clark, P. U. et al. The last glacial maximum. *Science* **325**, 710–714 (2009).
12. Abe-Ouchi, A. et al. Insolation-driven 100,000-year glacial cycles and hysteresis of ice-sheet volume. *Nature* **500**, 190–193 (2013).
13. Huybers, P. Combined obliquity and precession pacing of late Pleistocene deglaciations. *Nature* **480**, 229–232 (2011).
14. Parrenin, F. & Paillard, D. Terminations VI and VIII (∼530 and ∼720 kyr BP) tell us the importance of obliquity and precession in the triggering of deglaciations. *Clim. Past* **8**, 2031–2037 (2012).
15. Ganopolski, A. & Calov, R. The role of orbital forcing, carbon dioxide and regolith in 100 kyr glacial cycles. *Clim. Past* **7**, 1415–1425 (2011).
16. Kawamura, K. et al. Northern Hemisphere forcing of climatic cycles in Antarctica over the past 360,000 years. *Nature* **448**, 912–916 (2007).
17. Raymo, M. E. & Nisancioglu, K. H. The 41 kyr world: Milankovitch's other unsolved mystery. *Paleoceanography* **18**, 1011 (2003).
18. Shakun, J. D., Raymo, M. E. & Lea, D. W. An early Pleistocene Mg/Ca-δ18O record from the Gulf of Mexico: evaluating ice sheet size and pacing in the 41-kyr world. *Paleoceanography* **31**, 1011–1027 (2016).
19. Huybers, P. Early Pleistocene glacial cycles and the integrated summer insolation forcing. *Science* **313**, 508–511 (2006).
20. Huybers, P. & Tziperman, E. Integrated summer insolation forcing and 40,000-year glacial cycles: the perspective from an ice-sheet/energy-balance model. *Paleoceanography* **23**, PA001463 (2008).
21. Raymo, M. E., Lisiecki, L. E. & Nisancioglu, K. H. Plio-Pleistocene ice volume, Antarctic climate, and the global δ18O record. *Science* **313**, 492–495 (2006).
22. Tabor, C. R., Poulsen, C. J. & Pollard, D. How obliquity cycles powered early Pleistocene global ice-volume variability. *Geophys. Res. Lett.* **42**, 1871–1879 (2015).
23. Liautaud, P. R., Hodell, D. A. & Huybers, P. J. Detection of significant climatic precession variability in early Pleistocene glacial cycles. *Earth Planet. Sci. Lett.* **536**, 116137 (2020).
24. Vaucher, R. et al. Insolation-paced sea level and sediment flux during the early Pleistocene in Southeast Asia. *Sci. Rep.* **11**, 16707 (2021).
25. Sun, Y. et al. Persistent orbital influence on millennial climate variability through the Pleistocene. *Nat. Geosci.* **14**, 812–818 (2021).
26. Ashkenazy, Y. & Tziperman, E. Are the 41 kyr glacial oscillations a linear response to Milankovitch forcing? *Quat. Sci. Rev.* **23**, 1879–1890 (2004).
27. Lisiecki, L. E. & Raymo, M. E. Plio–Pleistocene climate evolution: trends and transitions in glacial cycle dynamics. *Quat. Sci. Rev.* **26**, 56–69 (2007).
28. Huybers, P. Glacial variability over the last two million years: an extended depth-derived agemodel, continuous obliquity pacing, and the Pleistocene progression. *Quat. Sci. Rev.* **26**, 37–55 (2007).
29. Barker, S. et al. Persistent influence of precession on northern ice sheet variability since the early Pleistocene. *Science* **376**, 961–967 (2022).
30. Abe-Ouchi, A., Segawa, T. & Saito, F. Climatic conditions for modelling the Northern Hemisphere ice sheets throughout the ice age cycle. *Clim. Past* **3**, 423–438 (2007).
31. Tabor, C. R., Poulsen, C. J. & Pollard, D. Mending Milankovitch's theory: obliquity amplification by surface feedbacks. *Clim. Past* **10**, 41–50 (2014).
32. O'ishi, R. & Abe-Ouchi, A. Influence of dynamic vegetation on climate change arising from increasing CO₂. *Clim. Dyn.* **33**, 645–CO663 (2009).
33. O'ishi, R. & Abe-Ouchi, A. Influence of dynamic vegetation on climate change and terrestrial carbon storage in the Last Glacial Maximum. *Clim. Past* **9**, 1571–1587 (2013).
34. Yan, Y. et al. Two-million-year-old snapshots of atmospheric gases from Antarctic ice. *Nature* **574**, 663–666 (2019).
35. Da, J., Zhang, Y. G., Li, G., Meng, X. & Ji, J. Low CO₂ levels of the entire Pleistocene epoch. *Nat. Commun.* **10**, 4342 (2019).
36. van de Wal, R. S. W., de Boer, B., Lourens, L. J., Köhler, P. & Bintanja, R. Reconstruction of a continuous high-resolution CO₂ record over the past 20 million years. *Clim. Past* **7**, 1459–1469 (2011).
37. Lisiecki, L. E. A benthic δ13C-based proxy for atmospheric pCO₂ over the last 1.5 Myr. *Geophys. Res. Lett.* **37**, L21708 (2010).
38. Yamamoto, M. et al. Increased interglacial atmospheric CO₂ levels followed the mid-Pleistocene Transition. *Nat. Geosci.* **15**, 307–313 (2022).
39. Hönisch, B., Hemming, N. G., Archer, D., Siddall, M. & McManus, J. F. Atmospheric carbon dioxide concentration across the mid-Pleistocene transition. *Science* **324**, 1551–1554 (2009).
40. de Boer, B., Lourens, L. J. & van de Wal, R. S. W. Persistent 400,000-year variability of Antarctic ice volume and the carbon cycle is revealed throughout the Plio-Pleistocene. *Nat. Commun.* **5**, 2999 (2014).
41. Pollard, D. & DeConto, R. M. Modelling West Antarctic ice sheet growth and collapse through the past five million years. *Nature* **458**, 329–332 (2009).

42. Sutter, J. et al. Modelling the Antarctic Ice Sheet across the mid-Pleistocene transition—implications for Oldest Ice. *The Cryosphere* **13**, 2023–2041 (2019).

43. Huybers, P. & Wunsch, C. Obliquity pacing of the late Pleistocene glacial terminations. *Nature* **434**, 491–494 (2005).

44. Paillard, D. The timing of Pleistocene glaciations from a simple multiple-state climate model. *Nature* **391**, 378–381 (1998).

45. Tzedakis, P. C. et al. Can we predict the duration of an interglacial? *Clim. Past* **8**, 1473–1485 (2012).

46. Wickert, A. D., Mitrovica, J. X., Williams, C. & Anderson, R. S. Gradual demise of a thin southern Laurentide ice sheet recorded by Mississippi drainage. *Nature* **502**, 668–671 (2013).

47. Balco, G., Rovey, C. W. II & Stone, J. O. H. The first glacial maximum in North America. *Science* **307**, 222 (2005).

48. Balco, G. & Rovey, C. W. II Absolute chronology for major Pleistocene advances of the Laurentide Ice Sheet. *Geology* **38**, 795–798 (2010).

49. Clark, P. U. & Pollard, D. Origin of the middle Pleistocene transition by ice sheet erosion of regolith. *Paleoceanography* **13**, 1–9 (1998).

50. Willeit, M., Ganopolski, A., Calov, R. & Brovkin, V. Mid-Pleistocene transition in glacial cycles explained by declining CO_2 and regolith removal. *Sci. Adv.* **5**, eaav7337 (2019).

51. Tzedakis, P. C., Crucifix, M., Mitsui, T. & Wolff, E. W. A simple rule to determine which insolation cycles lead to interglacials. *Nature* **542**, 427–432 (2017).

52. Lisiecki, L. E. Links between eccentricity forcing and the 100,000-year glacial cycle. *Nat. Geosci.* **3**, 349–352 (2010).

53. Tzedakis, P. C. et al. Interglacial diversity. *Nat. Geosci.* **2**, 751–755 (2009).

54. Yin, Q. Z. & Berger, A. Insolation and CO_2 contribution to the interglacial climate before and after the Mid-Brunhes Event. *Nat. Geosci.* **3**, 243–246 (2010).

55. Yin, Q. & Berger, A. Interglacial analogues of the Holocene and its natural near future. *Quat. Sci. Rev.* **120**, 28–46 (2015).

56. Past Interglacials Working Group of PAGES. Interglacials of the last 800,000 years. *Rev. Geophys.* **54**, 162–219 (2016).

57. Mitsui, T. & Boers, N. Machine learning approach reveals strong link between obliquity amplitude increase and the Mid-Brunhes transition. *Quat. Sci. Rev.* **277**, 107344 (2022).

58. Laskar, J. et al. A long-term numerical solution for the insolation quantities of the Earth. *Astron. Astrophys. Suppl. Ser.* **428**, 261–285 (2004).

59. Laskar, J., Fienga, A., Gastineau, M. & Manche, H. La2010: a new orbital solution for the long-term motion of the Earth. *Astron. Astrophys.* **532**, A89 (2011).

60. Hinnov, L. A. Cyclostratigraphy and its revolutionizing applications in the earth and planetary sciences. *GSA Bulletin* **125**, 1703–1734 (2013).

61. Chalk, T. B. et al. Causes of ice age intensification across the Mid-Pleistocene Transition. *Proc. Natl. Acad. Sci. USA* **114**, 13114–13119 (2017).

62. Seki, O. et al. Alkenone and boron-based Pliocene pCO_2 records. *Earth Planet. Sci. Lett.* **292**, 201–211 (2010).

63. Martínez-Botí, M. A. et al. Plio-Pleistocene climate sensitivity evaluated using high-resolution CO_2 records. *Nature* **518**, 49–54 (2015).

64. Dyez, K. A., Hönisch, B. & Schmidt, G. A. Early Pleistocene obliquity-scale pCO_2 variability at ~1.5 million years ago. *Paleoceanogr. Paleoclimatology* **33**, 1270–1291 (2018).

65. Ganopolski, A. & Brovkin, V. Simulation of climate, ice sheets and CO_2 evolution during the last four glacial cycles with an Earth system model of intermediate complexity. *Clim. Past* **13**, 1695–1716 (2017).

66. Kobayashi, H., Oka, A., Yamamoto, A. & Abe-Ouchi, A. Glacial carbon cycle changes by Southern Ocean processes with sedimentary amplification. *Sci. Adv.* **7**, eabg7723 (2021).

67. Berger, A., Li, X. S. & Loutre, M. F. Modelling northern hemisphere ice volume over the last 3 Ma. *Quat. Sci. Rev.* **18**, 1–11 (1999).

68. Huybers, P. & Langmuir, C. H. Delayed CO_2 emissions from mid-ocean ridge volcanism as a possible cause of late-Pleistocene glacial cycles. *Earth Planet. Sci. Lett.* **457**, 238–249 (2017).

69. Obase, T., Abe-Ouchi, A. & Saito, F. Abrupt climate changes in the last two deglaciations simulated with different Northern ice sheet discharge and insolation. *Sci. Rep.* **11**, 22359 (2021).

70. Köhler, P. Atmospheric CO_2 concentration based on boron isotopes versus simulations of the global carbon cycle during the Plio-Pleistocene. *Paleoceanog. Paleoclimatology* **38**, e2022PA004439 (2023).

71. Fischer, H. et al. Where to find 1.5 million yr old ice for the IPICS 'Oldest-Ice' ice core. *Clim. Past* **9**, 2489–2505 (2013).

72. Dahl-Jensen, D. Drilling for the oldest ice. *Nat. Geosci.* **11**, 703–704 (2018).

73. Hodell, D. et al. A 1.5-million-year record of orbital and millennial climate variability in the North Atlantic. *Clim. Past* **19**, 607–636 (2023).

74. O'ishi, R. & Abe-Ouchi, A. Polar amplification in the mid-Holocene derived from dynamical vegetation change with a GCM. *Geophys. Res. Lett.* **38**, L14702 (2011).

75. O'ishi, R. et al. PMIP4/CMIP6 last interglacial simulations using three different versions of MIROC: importance of vegetation. *Clim. Past* **17**, 21–36 (2021).

76. K-1 Model Developers. *K-1 Coupled GCM (MIROC) Description*. K-1 Technical Report. Vol. 1, 1–34 (2004).

77. Berger, A. & Loutre, M. F. Insolation values for the climate of the last 10 million years. *Quat. Sci. Rev.* **10**, 297–317 (1991).

78. Higgins, J. A. et al. Atmospheric composition 1 million years ago from blue ice in the Allan Hills, Antarctica. *Proc. Natl. Acad. Sci. USA* **112**, 6887–6891 (2015).

79. Virtanen, P. et al. SciPy 1.0: fundamental algorithms for scientific computing in Python. *Nat. Methods* **17**, 261–272 (2020).

80. Upton, G. & Fingleton, B. *Spatial Data Analysis by Example* Vol. 2 (John Wiley and Sons, 1989).

81. Grinsted, A., Moore, J. C. & Jevrejeva, S. Application of the cross wavelet transform and wavelet coherence to geophysical time series. *Nonlinear Process. Geophys.* **11**, 561–566 (2004).

82. Berger, A. Long-term variations of daily insolation and quaternary climatic changes. *J. Atmos. Sci.* **35**, 2362–2367 (1978).

83. Bereiter, B. et al. Revision of the EPICA Dome C CO_2 record from 800 to 600 kyr before present. *Geophys. Res. Lett.* **42**, 542–549 (2015).

84. Köhler, P. & van de Wal, R. S. W. Interglacials of the Quaternary defined by northern hemispheric land ice distribution outside of Greenland. *Nat. Commun.* **11**, 5124 (2020).

85. Spratt, R. M. & Lisiecki, L. E. A Late Pleistocene sea level stack. *Clim. Past* **12**, 1079–1092 (2016).

Author contributions

Conceptualization: A.A. and Y.W.; supervision: A.A.; methodology: A.A., Y.W. and F.S.; software: F.S. and Y.W.; data curation: Y.W., F.S. (IcIES-MIROC), K.Ki. and R.O. (MIROC-LPJ); visualization: Y.W.; funding acquisition: A.A.; writing—original draft: Y.W. and A.A.; writing—review & editing: Y.W., A.A., F.S., T.I., K.Ka., W.L.C., K.Ki. and R.O.

Competing interests

The authors declare no competing interests.

Additional information

Supplementary information The online version contains supplementary material available at https://doi.org/10.1038/s43247-023-00765-x.

Correspondence and requests for materials should be addressed to Ayako Abe-Ouchi.

Peer review information *Communications Earth & Environment* thanks Polychronis Tzedakis and the other, anonymous, reviewer(s) for their contribution to the peer review of this work. Primary Handling Editors: Kyung-Sook Yun and Aliénor Lavergne.

Reprints and permission information is available at http://www.nature.com/reprints

Publisher's note Springer Nature remains neutral with regard to jurisdictional claims in published maps and institutional affiliations.